Vapor phase fabrication of nanoheterostructures based on ZnO for photoelectrochemical water splitting

WILEY-VCH

DOI: 10.1002/ ((please add manuscript number))
Article type: Full paper

Vapor phase fabrication of nanoheterostructures based on ZnO for photoelectrochemical water splitting

By *Davide Barreca, Giorgio Carraro, Alberto Gasparotto, Chiara Maccato,* Thomas Altantzis, Cinzia Sada, Kimmo Kaunisto, Tero-Petri Ruoko, and Sara Bals*

Dr. D. Barreca
CNR-ICMATE and INSTM, Department of Chemistry, Padova University, 35131 Padova, Italy.

[*] Dr. G. Carraro, Prof. A. Gasparotto, Prof. C. Maccato
Department of Chemistry, Padova University and INSTM, 35131 Padova, Italy.
E-mail: chiara.maccato@unipd.it

Dr. T. Altantzis, Prof. S. Bals
EMAT, University of Antwerp, 2020 Antwerpen, Belgium.

Prof. C. Sada
Department of Physics and Astronomy, Padova University, 35131 Padova, Italy.

Dr. K. Kaunisto, Dr. T.-P. Ruoko
Department of Chemistry and Bioengineering, Tampere University of Technology, 33101 Tampere, Finland.

Keywords: ZnO; Fe_2O_3; WO_3; nanoheterostructures; water splitting.

Abstract: Nanoheterostructures based on metal oxide semiconductors have emerged as promising materials for the conversion of sunlight into chemical energy. In the present study, ZnO-based nanocomposites have been developed by a hybrid vapor phase route, consisting in the chemical vapor deposition of ZnO systems on fluorine-doped tin oxide substrates, followed by the functionalization with Fe_2O_3 or WO_3 *via* radio frequency-sputtering. The target systems were subjeted to thermal treatment in air both prior and after sputtering, and their properties, including structure, chemical composition, morphology and optical absorption, were investigated by a variety of characterization methods. The obtained results evidenced the formation of highly porous ZnO nanocrystal arrays, conformally covered by an ultrathin Fe_2O_3 or WO_3 overlayer. Photocurrent density measurements for solar-triggered water splitting revealed in both cases a performance improvement with respect to bare zinc oxide, that was mainly traced back to an enhanced separation of photogenerated charge carriers thanks to the intimate contact between the two oxides. This achievement can be regarded as a valuable result in view of future optimization of similar nanoheterostructured photoanodes.

1. Introduction

Over the last decades, the utilization of sunlight-assisted semiconductor photocatalysis for pollutant degradation, as well as for hydrogen production from water has gained considerable momentum, due to the increasing concern on environmental and energy issues.[1-8] In particular, photoelectrochemical (PEC) water splitting[9-12] stands as a promising route for the renewable conversion of solar light into storable and clean chemical energy with zero carbon emission.[13-21] Up to date, a great deal of attention has been dedicated to the development of various oxide photoanodes for these applications (TiO_2, WO_3, ZnO, Fe_2O_3, $BiVO_4$, …),[7,10,12-16,18,22-31] especially in nanostructured forms in order to attain improved system performances.[11,20,26,32] In this regard, ZnO, a transparent semiconducting oxide with a large exciton binding energy (60 meV) and high carrier mobility, has attracted an extensive interest.[5,15,18,32-34] Nevertheless, its performances are detrimentally affected by its wide band gap (E_G = 3.3 eV),[3,14,35-39] limiting radiation absorption to the UV interval (≈5% of the overall solar spectrum),[1,2,38,40-43] and by the rapid charge carriers recombination.[33,35-37,44] To tackle these obstacles and extend the system photoresponse into the Vis range,[1,15,39] various investigators have been focused on doping with substitutional elements to the Zn and O sites.[3,21,32,40,41,43] Appreciable efforts have also been devoted to the coupling of ZnO with other suitable semiconductors, with the aim to tailor their interfacial energetics to the targeted photoactivated processes.[2,22,27,36,45,46] In this regard, various heterojunction-containing composites based on ZnO-TiO_2,[8] ZnO-NiO,[31] ZnO-CdS,[11] ZnO-CdSe,[34] ZnO-CdTe,[43] ZnO-$M(OH)_x$ with M = Co, Ni,[16] ZnO-$BiVO_4$,[42] ZnO-WO_x coupled with CdSe-CdS,[45] ZnO-ZnS-FeS_2,[39] and ZnO-CdS-NiO[17] have been developed and tested for solar-driven H_2O splitting. In this broad scenario, an attractive option involves the use of Fe_2O_3 and WO_3 as functional activators of ZnO systems for the fabrication of Vis-light absorbing photoanodes. In particular, Fe_2O_3, an abundant and cheap oxide with a narrow band gap (E_G = 2.2 eV),[9,26,28,35] has gained a considerable attention, but its sluggish oxygen evolution

kinetics, low carrier lifetime and short exciton diffusion length limit the resulting functional performances.[13,18,28,31,47] Another attractive material not only for solar water splitting, but also for environmental remediation, is WO_3,[2,6,19] which possesses an appreciable photostability and a favorable band gap (E_G = 2.8 eV).[3,12,22,27,29,30,37] Nevertheless, the indirect nature of this band gap results in optical pathways corresponding to Vis wavelengths that are at least one order of magnitude higher than the hole diffusion length (≈0.15 μm),[29] requiring the use of tailored nanosystems to improve functional performances. In this scenario, the development ZnO-Fe_2O_3 and ZnO-WO_3 nanoheterostructures, in which ZnO nanosystems are functionalized with Fe_2O_3 or WO_3 particles or overlayers, would concurrently provide a valuable route to engineer the system performances and compensate individual material drawbacks, such as ZnO photocorrosion.[48] In particular, the broader light absorption range and restrained carrier recombination are key advantages for the improvement of PEC H_2 generation.[9,13,35,37,38,49] Nevertheless, up to date ZnO-Fe_2O_3 and ZnO-WO_3 composites have been mainly used for gas sensing[50-52] and photocatalytic pollutant degradation,[3,35,37,38,44,49] whereas only a few reports have been dedicated to their applications in PEC water splitting.[14,27,45] These observations highlight the urgent need of viable preparation routes to supported ZnO-Fe_2O_3 and ZnO-WO_3 nanosystems, allowing a fine control over their morphology and interface structure.[22,38]

Taking into account these evidences, the investigation performed in the present work aims at providing a contribution in this direction, being addressed to the fabrication and characterization of ZnO-based nanoheterostructures for solar-driven water splitting. Following our previous works on multi-component oxide-based nanomaterials,[47,53-56] herein we propose a highly controllable preparation strategy for the fabrication of ZnO-Fe_2O_3 and ZnO-WO_3 nanoheterostructures, consisting in the chemical vapor deposition (CVD) of ZnO on fluorine-doped tin oxide (FTO) and in the subsequent radio frequency (RF)-sputtering of Fe_2O_3 or WO_3 onto the obtained systems under mild operational conditions. Particular efforts

were specifically dedicated to the uniform decoration of ZnO nanostructures by Fe_2O_3 or WO_3 overlayers and to the obtainment of an intimate oxide-oxide contact, in order to synergistically exploit the combination of the single component properties. To this regard, a multi-technique investigation was carried out through the use of complementary analytical tools, in order to shed light on the system nanostructure, morphology, composition and optical properties. Finally, a preliminary investigation on the system performances in PEC water splitting promoted by simulated solar light was carried out, discussing the possible causes for the performance enhancement brought about by ZnO functionalization with Fe_2O_3 and WO_3 and providing a possible strategy to achieve enhanced functional performances. To the best of our knowledge, the preparation of the target systems by the proposed route for PEC water splitting has never been reported in the literature up to date.

2. Results and Discussion

In this work, ZnO-Fe_2O_3 and ZnO-WO_3 photoanodes were developed by means of a multi-step synthetic strategy, involving: (a) CVD of ZnO on FTO substrates; (b) RF-sputtering of Fe_2O_3 or WO_3 onto the obtained systems. For comparison purposes, relevant properties of bare ZnO were also investigated (see also the Supporting Information).

Preliminary information on the system structure was obtained by glancing incidence X-ray diffraction (GIXRD). As can be observed in Figure 1, the recorded patterns were dominated by peaks located at 2ϑ = 31.7, 34.4, 36.2, and 47.5°, related respectively to the (100), (002), (101) and (102) reflections of the *wurtzite* ZnO crystalline phase.[57] Irrespective of the processing conditions, the $I_{(002)}/I_{(101)}$ intensity ratio (Supporting Information, Figure S1) was always higher than that of the reference powder spectrum, suggesting the occurrence of a preferred orientation along the *c*-axis (*i.e.*, with the <001> direction almost perpendicular to the substrate).[58] This phenomenon could be related to the ZnO *wurtzite* structure, composed of alternate O and Zn crystallographic planes stacked along the *c* axis. The spontaneous

polarization along this direction promotes the occurrence of the (001) orientation, due to the tendency to satisfy the decrease in the overall free energy.[59] In the present case, this phenomenon was further boosted by the introduction of water vapor, producing a preferential interaction of –OH groups with the Zn(II)-terminated (001) polar ZnO surface. This effect, in turn, enhances precursor decomposition and favors a preferential growth along this direction. Nevertheless, the concomitant hydroxyl interaction with other ZnO surfaces was responsible for a lateral growth competitive with the previous one, accounting thus for the appearance even of the other diffraction peaks and not only of the (002) one.

For the composite samples, no additional signals related to crystalline Fe_2O_3 or WO_3 or mixed Zn-Fe-O/Zn-W-O phases could be observed. In line with previous works on multi-component oxide nanosystems obtained by analogous routes,[47,53-56] this result could be related to the low Fe_2O_3/WO_3 loading, as confirmed by transmission electron microscopy (TEM) data (see below and Figure 4), and suggested that the adopted processing conditions were mild enough to avoid significant structural alterations of the pristine ZnO matrix. The main difference for ZnO-Fe_2O_3 and ZnO-WO_3 systems with respect to bare ZnO was the slightly lower $I_{(002)}/I_{(101)}$ intensity ratio (Supporting Information, Figure S1). The mean ZnO crystallite size was evaluated to be 30 nm and did not undergo any significant alteration upon Fe_2O_3 and WO_3 deposition.

The surface chemical composition was analyzed by X-ray photoelectron and X-ray excited Auger photoelectron spectroscopies (XPS and XE-AES). Survey spectra confirmed the successful Fe_2O_3 and WO_3 deposition onto ZnO (Supporting Information, Figure S2), with no other impurity within the technique detection limit, apart from adventitious carbon. In all cases, the surface presence of zinc could also be observed (see Figure 2a), a phenomenon traced back to ZnO coverage by ultrathin and porous Fe_2O_3/WO_3 overlayers (compare field emission scanning electron microscopy (FE-SEM) and TEM analyses, see below). The $Zn2p_{3/2}$ binding energy (BE) was 1022.0 eV for pure ZnO, in line with literature

data,[5,31,48,60,61] whereas it underwent a slight downward (1021.9 eV) and upward (1022.3 eV) shift for ZnO-Fe_2O_3 or ZnO-WO_3 samples, respectively. This phenomenon can be explained taking into account that, at the interface between ZnO and Fe_2O_3 nanoaggregates, the equilibration of the energy levels leads to a higher position for the Fe_2O_3 conduction band (CB) edge with respect to the ZnO one.[1,9,13] This phenomenon, in turn, promotes an electron transfer from Fe_2O_3 to ZnO CB, accounting for the lower BE value of $Zn2p_{3/2}$ in ZnO-Fe_2O_3. In line with these observations, the position of the Fe2p spin-orbit components [Figure 2b; BE($Fe2p_{3/2}$) = 711.4 eV; spin-orbit splitting = 13.7 eV] was slightly higher than that reported for Fe_2O_3.[1,9,24,47,53] In a different way, the opposite situation holds for the mutual CB edge positions at the ZnO-WO_3 interface, so that the electron flow direction is expected to be from ZnO to WO_3 when the two systems are in contact.[27,36-38,44] As a consequence, the measured BE($Zn2p_{3/2}$) in the case of ZnO-WO_3 nanoheterostructures was higher than for the pristine ZnO (see above). The position of the W4f photopeak [BE($W4f_{7/2}$) = 35.6 eV] (Figure 2c), slightly lower than previous literature data for W(VI) oxide,[12,53,61] validated the above hypothesis. Overall, the obtainment of ZnO/Fe_2O_3 and ZnO/WO_3 interfaces with tunable features appears very promising for a possible improvement of the system functional properties in PEC water splitting, as described below. Quantitative analyses enabled to calculate the W and Fe surface molar fraction, yielding a mean value of X_M = 0.63 (M = Fe, W) for both ZnO-Fe_2O_3 and ZnO-WO_3 systems.

In all cases, evaluation of the zinc Auger parameter always yielded α = 2010.6 eV, providing thus a finger-print for the presence of ZnO free from other Zn-containing phases, irrespective of the processing conditions.[60] This conclusion, in agreement with the above discussed XRD data, was further corroborated by TEM results (see below and Figure 4).

Concerning bare ZnO, the surface O1s peak (Figure 2d) was characterized by a main component located at BE = 530.1 eV, related to lattice oxygen in ZnO,[3,27,33,59] and a tailing towards higher BE with a shoulder at ≈532.0 eV, attributed to surface –OH groups saturating

O vacancies.[3,24,53,54] The presence of these defects is expected to favorably influence the system PEC performances, resulting in an improved charge transportation and in a photocurrent density enhancement.[33] In the case of ZnO-Fe_2O_3, the main O1s component underwent a shift towards lower BEs, due to the contribution of lattice oxygen in Fe_2O_3, expected at 529.8 eV.[10,47,55] Conversely, the opposite O1s peak shift took place for the ZnO-WO_3 specimen, since the O signal for WO_3 is located at 530.5 eV.[27,61]

The in-depth system composition was investigated by secondary ion mass spectrometry (SIMS) analysis, that enabled to estimate a carbon concentration of ≈100 ppm (averaged over the whole nanodeposit thickness), demonstrating thus the purity of the obtained materials. Representative profiles (Supporting Information, Figure S3) revealed an almost constant oxygen ionic yield throughout the sampled depth. The analysis of Zn, W and Fe signals revealed that Fe and W were mainly concentrated in the near-surface zone. In addition, the appreciable Fe and W signal tailing towards the interface with the FTO substrate suggested an efficient ZnO coverage by Fe_2O_3 (or WO_3) even in the inner system regions, thanks to the porosity characterizing the pristine ZnO nanodeposits [see also high angle annular dark field scanning TEM (HAADF-STEM) and STEM energy dispersive X-ray spectroscopy (STEM-EDXS) analysis for further details]. The present results, in line with recent reports on oxide nanocomposites obtained by hybrid vapor phase approaches,[24,55,56] indicate the successful achievement of an intimate contact between the target ZnO nanosystem and the Fe_2O_3 (or WO_3) overlayer. The latter phenomenon accounts for the electronic interplay between the system component already discussed in relation to XPS data (see above), and plays a crucial role in determining the photoresponse of ZnO-Fe_2O_3 and ZnO-WO_3 nanoheterostructures in PEC water splitting (compare Figure 5 and the pertaining data discussion). Finally, the recorded SIMS profiles evidenced a certain Sn inter-diffusion from the FTO substrates into the target nanosystems, an effect that has been reported to positively influence charge transport phenomena and, ultimately, PEC performances.[24,47]

The system morphology and nano-organization were analyzed by FE-SEM. Plane-view investigation showed that bare ZnO (Supporting Information, Figure S4) was characterized by the presence of homogeneously distributed and highly interconnected "wavy" nanoaggregates (mean lateral size = 100 ± 20 nm), resulting in a porous material extremely favourable for the subsequent dispersion of Fe_2O_3 and WO_3. The deposition of Fe_2O_3 or WO_3 induced no appreciable morphological variations on the zinc oxide host matrix (see Figure 3), confirming thus that the adopted synthetic approach preserved the nanorganization of the underlying metal oxide. For both bare ZnO and nanocomposite materials, similar mean thickness values of (120 ±30) nm were estimated, in line with the deposited small amount of Fe_2O_3 and WO_3. In the case of ZnO-WO_3 system, taking advantage of the different Z values of the metal centers in the two oxides, the homogeneous distribution of tungsten oxide over ZnO nanostructures was confirmed by the image recorded collecting backscattered electrons (Figure 3c).

In order to shed further light into the nanoscale structure of ZnO-Fe_2O_3 and ZnO-WO_3 materials, HAADF-STEM and EDXS analyses were carried out. Figures 4a-d display HAADF-STEM overview cross-sectional images of composite systems, together with the related EDXS elemental maps for Fe, W, Zn, Sn and Si. In both cases, the presence of glass/FTO/ZnO/Fe_2O_3 or WO_3 multilayer stacks was clearly evident. EDXS spectra acquired from the regions shown in Figures 4a-b are presented in Supporting Information, Figure S5. The presence of dark contrast voids in the ZnO aggregates (Figures 4e-f) highlights a certain system porosity. High resolution HAADF-STEM images from the ZnO-Fe_2O_3 and ZnO-WO_3 interfaces are shown in Figures 4g-h, clearly revealing the successful formation of oxide-oxide nanoheterostructures. In particular, as can be observed, a conformal coverage of the ZnO surface by Fe_2O_3 and WO_3 layers was obtained, and their very low thickness (a few nm) prevented their clear detection by FE-SEM.[54]

From the high resolution HAADF-STEM images and the corresponding fast Fourier

transform (FFT) patterns, it could be observed that for the ZnO-Fe_2O_3 sample the Fe_2O_3 overlayer is crystalline, and the observed reflections could be attributed to γ-Fe_2O_3 (*maghemite*).[62] The formation of this polymorph, instead of the most thermodynamically stable one, α-Fe_2O_3 (*hematite*), could be traced back to the unique non-equilibrium plasma conditions characterizing RF-sputtering.[47] In a different way, for the ZnO-WO_3 system, the WO_3 overlayer resulted amorphous, similarly to other sputtered oxides produced by a similar hybrid synthetic route.[55] In both cases, the FFTs of the ZnO crystals (Figures 4g-h) could be indexed according to the hexagonal *wurtzite* phase.[57] No Zn-Fe-O or Zn-W-O ternary phases were detected, in line with the fact that the thermally-induced formation of $ZnFe_2O_4$ ($ZnWO_4$) has been reported to occur at temperatures higher than the ones used in the present investigation (see the Experimental Section).[10,14,26,63,64]

The final aim of this work was the functional validation of ZnO, ZnO-Fe_2O_3 and ZnO-WO_3 nanosystems as photoanodes in sunlight-assisted PEC water splitting. To this regard, Figure 5a displays photocurrent density *vs.* potential curves recorded under direct illumination. Although being lower than those reported for photoanodes based on other materials, such as Fe_2O_3,[24] the photocurrents recorded for bare ZnO (30 μA/cm^2 at 0.8 V *vs.* Ag/AgCl) compared favourably with those pertaining to other zinc(II) oxide systems tested under similar experimental conditions,[20,21,31,40-42,65] and could be mainly traced back to the high area and inherent porosity of the present ZnO nanoaggregates (see above). This finding highlights the potential of the proposed fabrication route for the production of ZnO anodes with a reasonable photoresponse even without the introduction of any further dopant or activator. Interestingly, a comparison of the pristine ZnO curve with those pertaining to ZnO-Fe_2O_3 and ZnO-WO_3 nanoheterostructures evidenced that ZnO functionalization was an effective mean to increase the recorded photocurrents, particularly at high applied potentials, although the photoactivity enhancement was different in the two cases. In fact, Fe_2O_3 was

responsible for an improvement close to 15% (35 μA/cm^2 at 0.8 V *vs*. Ag/AgCl), whereas WO_3 introduction resulted in a nearly two-fold photocurrent increase (≈55 μA/cm^2 at 0.8 V *vs*. Ag/AgCl). Irrespective of the overlayer nature, an important result was the absence of saturation at potentials higher than 0.8 *vs*. Ag/AgCl, which was attributed to the formation of ZnO/Fe_2O_3 or ZnO/WO_3 heterojunctions, responsible, in turn, for a more efficient photocarrier separation with respect to bare ZnO.[24] To further demonstrate the beneficial role of Fe_2O_3 and WO_3 functionalization, it is worthwhile highlighting that the PEC response of iron(III) and tungsten(VI) oxides, deposited on FTO substrates under the same conditions used to prepare the composite systems, was appreciably lower (Supporting Information, Figure S7).

In an attempt to investigate the stability of the present materials, PEC measurements were repeated under the same experimental conditions at the first and third day for both composite systems, similarly to our previous study.[24] The corresponding results (Supporting Information, Figure S8) revealed that the measured photocurrent values did not undergo significant variations upon prolonged utilization. This evidence enabled to rule out the occurrence of relevant photocorrosion/degradation phenomena under the adopted conditions and suggested a good stability of the target photoanodes, an important issue for their ultimate functional applications.

As a matter of fact, the increased PEC performances of heterostructured systems with respect to bare ZnO cannot be rationalized basing only on the mutual CB positions of the single oxide components.[4,6,14,18,35,36,49] Indeed, in the case of ZnO-Fe_2O_3 systems, the equilibration of the quasi-Fermi levels at the interface between the two oxides leads to a higher energy position of the Fe_2O_3 CB edge with respect to ZnO one (Figure 5b).[1,9,13] As a consequence, upon the formation of photoexcited electron–hole pairs, electrons can be transferred from Fe_2O_3 to ZnO CB and, at the same time, an increased number of photo-holes become available at the photoanode surface to promote water oxidation. This explanation, that is in line with the

already discussed XPS results (see above), accounts for the observed enhancement in photocurrent density of ZnO-Fe_2O_3 photoanodes in comparison to the pristine bare ZnO. It is worthwhile noticing that, in this regard, the loading and distribution of Fe_2O_3 species need to be finely tuned. A higher Fe_2O_3 amount can, on one side, promote the formation of a higher number of photogenerated electrons-holes pairs, but, on the other side, be responsible for an increased recombination rate.[13] Hence, further photocurrent improvements are strongly dependent on a fine counterbalance of these effects, that might be achieved by the optimization of the Fe_2O_3 overlayer, as well as of the underlying ZnO system.[13]

Regarding ZnO-WO_3 nanoheterostructures, the increased PEC performances of ZnO-WO_3 with respect to bare ZnO can be explained considering that, upon irradiation, an increase of the WO_3 quasi-Fermi level may be originated by the injection of electrons in its CB. This, in turn, could reverse the charge transfer mechanism in comparison to that expected basing on the mutual band edge positions. On this basis, electrons in the WO_3 CB can migrate to ZnO surface, to which the anodic potential is applied, and subsequently be transferred through the external circuit to the counterelectrode. On the other hand, free holes in WO_3 can oxidize water (see Figure 5c). A similar mechanism has been proposed for TiO_2 nanosystems coated by a WO_3 overlayer,[22] and can be reasonably extended to ZnO-WO_3 nanoheterostructures considering the similar E_G and band edge positions of TiO_2 and ZnO.[6,20]

3. Conclusions

In this work, we have successfully prepared ZnO-Fe_2O_3 and ZnO-WO_3 nanoheterostructures by means of a combined CVD/RF-sputtering route. A detailed multi-technique characterization evidenced the formation of porous ZnO nanostructures conformally covered by Fe_2O_3 or WO_3 overlayers, characterized by an intimate contact between the single oxides. A proper tuning of the processing conditions enabled the obtainment of similar thickness values of Fe_2O_3 and WO_3 overlayers. Whereas the latter was revealed to be amorphous, the

former comprised the γ-Fe_2O_3 (*maghemite*) crystal structure. Functional tests in solar-driven PEC H_2O splitting, carried out for the first time on ZnO-Fe_2O_3 and ZnO-WO_3 systems fabricated by the proposed route, evidenced a favorable performance increase, that was traced back to an improved charge carrier separation enhancing the system photoresponse.

The present results disclose interesting perspectives in view of further optimization of the obtained performances through a tailored engineering of the Fe_2O_3 or WO_3 overlayers.

Under the present conditions, the introduction of WO_3, despite the higher E_G, has been proved to be more effective than that of Fe_2O_3 in boosting PEC performances. On the other hand, considering the different charge carrier transfer mechanisms occurring in the two cases, a further optimization of material performances would probably require the use of different strategies as a function of the overlayer nature. In order to attain a detailed insight on the photoanode efficiency and stability as a function of the target heterojunction properties, the present specimens will be the focus of further advanced studies, involving also the analysis of incident photon-to-current efficiency (IPCE) and the use of chronoamperometry measurements. In any case, the information reported herein may offer novel hints for further contribution to high efficiency and low-cost photoelectrode processing for solar-assisted PEC water splitting.

4. Experimental Section

4.1 Synthesis

ZnO-Fe_2O_3 and ZnO-WO_3 nanoheterostructures were obtained by means of a multi-step vapor phase process. In particular, ZnO nanosystems were fabricated by a custom-built hot-wall (HW) CVD reactor, equipped with a Carbolite HST 12/200 tubular furnace and a tubular quartz reaction chamber (inner diameter = 9.5 cm, length of the heated region = 20 cm).[53] Depositions were carried out on FTO-coated glass substrates (Aldrich®, 735167-1EA, ≈7 Ω/sq, lateral dimensions = 2.0 cm × 1.0 cm; FTO thickness = 600 nm), pre-cleaned according to a well-established procedure.[56] $Zn(hfa)_2TMEDA$ (hfa = 1,1,1,5,5,5 - hexafluoro - 2,4 - pentanedionate, TMEDA = *N*,*N*,*N*′,*N*′ - tetramethylethylenediamine) was chosen as Zn precursor and synthesized according to the literature.[58]

In a typical experiment, precursor powders (1.2 g) were vaporized in an external glass reservoir maintained at 80°C, and vapor transport into the reaction chamber was performed through gas lines heated at 120°C by means of an N_2 flow (purity = 6.0, rate = 100 sccm). An additional oxygen flow (purity = 6.0, rate = 30 sccm) was introduced separately into the reactor after passing through a water reservoir maintained at 30°C. On the basis of preliminary results, growth processes were performed under optimized conditions (total pressure = 3.0 mbar, substrate temperature 450°C, experiment duration = 120 min). After deposition, the as-prepared ZnO specimens were subjected to *ex-situ* thermal treatments at 550°C for 3 h, carried out in air and at atmospheric pressure using a Carbolite HST 12/200 tubular oven. This pre-annealing treatment of bare ZnO, carried out in order to improve the system crystallinity and reduce grain boundary content, was reported to produce a net photoactivity enhancement.[8]

Subsequently, ZnO systems were functionalized with Fe_2O_3 and WO_3 overlayers by RF-sputtering, using a two-electrode custom-built reactor equipped with an RF-generator (ν = 13.56 MHz).[66] Experiments were conducted using electronic grade Ar plasmas, starting from

Fe (Alfa Aesar®, purity = 99.995%, thickness = 2 mm, 50×50 mm) and WO_3 targets (Neyco®, purity = 99.99%, thickness = 2 mm, diameter = 2 in;) fixed on the RF-electrode, whereas FTO-supported ZnO samples were placed on the grounded electrode. For both Fe_2O_3 and WO_3, sputtering experiments were carried out using optimized conditions (Ar flow rate = 10 sccm, total pressure = 0.3 mbar; RF-power = 20 W, duration = 3 h, grounded electrode temperature = 60°C, inter-electrode distance = 5 cm). Basing on preliminary XPS analyses, these experimental settings were chosen in order to obtain a comparable loading of Fe_2O_3 and WO_3 over the pristine ZnO nanodeposits. The use of harsher plasma conditions in sputtering processes was intentionally discarded to prevent the obtainment of too compact systems with reduced active area, a feature that might negatively influence the system functional behavior.[24,54] For PEC control experiments, bare Fe_2O_3 and WO_3 nanodeposits were prepared by sputtering on FTO under the above described conditions.

After sputtering, the obtained systems were subjected to *ex-situ* thermal treatments, in order to attain a complete Fe oxidation, for Fe_2O_3-containing systems, and a proper material stabilization before functional tests, for both ZnO-Fe_2O_3 and ZnO-WO_3 nanoheterostructures. This annealing step was carried out in air for 1 h at 350°C, avoiding the use of higher temperatures in order to prevent the formation of ternary phases.[10,14,26,63,64]

4.2 Characterization

The deposit mass was measured by using a Mettler Toledo XS105DU Microbalance, yielding a mean value of (0.20 ± 0.03) mg.

GIXRD patterns were recorded at a fixed incidence angle of 1.0° by means of a Bruker D8 Advance diffractometer equipped with a Göbel mirror, using a CuKα X-ray source powered at 40 kV and 40 mA. The mean crystallite sizes were estimated using the Scherrer equation.

Surface XPS and XE-AES analyses were carried out using a Perkin-Elmer Φ 5600ci instrument using a standard MgKα radiation (hν = 1253.6 eV), at working pressures < 10^{-8}

mbar. The element BE values were corrected for charging by assigning a position of 284.8 eV to the C1s signal arising from adventitious contamination.[60,61] Atomic percentages (at. %) were calculated through peak integration, using standard PHI V5.4A sensitivity factors. Zn Auger parameter was defined as α = BE($Zn2p_{3/2}$) + KE (ZnLMM). Surface Fe and W molar fractions were calculated as X_M = (M at.%)/[(M at.%) + (Zn at.%)]×100, with M = Fe, W.[47,53]

In-depth SIMS analyses were performed by means of a IMS 4f mass spectrometer (Cameca) using a Cs^+ primary beam (voltage = 14.5 KeV, current =20 nA, stability = 0.2%) and by negative secondary ion detection, using an electron gun to compensate for charging effects. Signals were detected in beam blanking mode and high mass resolution configuration, rastering over a 150×150 μm^2 area and sampling secondary ions from a 7×7 μm^2 sub-region.

FE-SEM images were collected by a Zeiss SUPRA 40 VP apparatus, using InLens and back-scattered electron detectors. Plane-view and cross-sectional micrographs were recorded with a primary beam voltage of 10.0 kV. The mean nanoaggregate size and deposit thickness values were estimated by using the ImageJ® (http://imagej.nih.gov/ij/, accessed September 2016) picture analyzer software by averaging over 30 independent measurements.

Samples for cross-sectional TEM observations were prepared by Ar^+ ion milling. To this aim, specimens were first mechanically polished using an Allied Multiprep System with diamond-lapping films, up to a thickness of approximately 20 μm, followed by fine Ar^+ ion milling by using a Leica EM RES102 with acceleration voltages up to 4 kV and incident beam angles between 6° and 11°. Low and high magnification HAADF-STEM images as well as EDXS elemental maps were acquired by using an aberration corrected cubed FEI Titan electron microscope operated at 300 kV, equipped with the ChemiSTEM[67] system. For HAADF-STEM imaging, a probe convergence semi-angle and a detector's inner collection semi-angle of 21 and 55 mrad, respectively, were used.

Photocurrent/voltage measurements were performed using a three-electrode electrochemical

system, with a Pt counterelectrode and an Ag/AgCl (3 M NaCl) reference electrode. Prior to each measurement the electrolyte, an aqueous solution containing 0.5 M Na_2SO_4, was purged with flowing N_2 in order to remove dissolved oxygen.[24,47] The working electrode geometric area (1.3 ± 0.1 cm^2) was estimated using a microscope controlled *via* a computer software. Cyclic voltammograms were recorded, both in the dark and under front side illumination, at a fixed scan rate of 10 $mV \times s^{-1}$ in the potential sweep range of -0.4/1.2 V *vs*. Ag/AgCl. Specimens were irradiated with simulated sunlight from a 450 W Xe lamp equipped with a KG3 filter (Thorlabs). The light intensity was set to match $100mW \times cm^{-2}$ AM1.5G spectrum. Dark currents (not reported) were two orders of magnitude lower than those obtained under illumination.

Supporting Information

Supporting Information is available from the Wiley Online Library or from the authors.

Acknowledgements

The authors kindly acknowledge the financial support under Padova University ex-60% 2013-2016, P-DiSC #SENSATIONAL BIRD2016-UNIPD projects and the post-doc fellowship ACTION. S.B. acknowledges financial support from the European Research Council (Starting Grant No. COLOURATOM 335078) and T.A. acknowledges funding from the Research Foundation Flanders (FWO, Belgium) through a postdoctoral grant. Many thanks are also due to Dr. Rosa Calabrese (Department of Chemistry, Padova University, Italy) for experimental assistance.

References

[1] G. K. Pradhan, S. Martha, K. M. Parida, *ACS Appl. Mater. Interfaces* **2012**, *4*, 707.

[2] A. Thomas, C. Janáky, G. F. Samu, M. N. Huda, P. Sarker, J. P. Liu, V. van Nguyen, E. H. Wang, K. A. Schug, K. Rajeshwar, *ChemSusChem* **2015**, *8*, 1652.

[3] S.-M. Lam, J.-C. Sin, A. Z. Abdullah, A. R. Mohamed, *J. Colloid Interface Sci.* **2015**, *450*, 34.

[4] D. Li, H. Haneda, *J. Photochem. Photobiol., A* **2003**, *160*, 203.

[5] D. M. Fragua, R. Abargues, P. J. Rodriguez-Canto, J. F. Sanchez-Royo, S. Agouram, J. P. Martinez-Pastor, *Adv. Mater. Interfaces* **2015**, *2*, 1500156.

[6] H. Zhang, G. Chen, D. W. Bahnemann, *J. Mater. Chem.* **2009**, *19*, 5089.

[7] W. Chen, Y. Qiu, S. Yang, *Phys. Chem. Chem. Phys.* **2012**, *14*, 10872.

[8] S. Hernández, V. Cauda, A. Chiodoni, S. Dallorto, A. Sacco, D. Hidalgo, E. Celasco, C. F. Pirri, *ACS Appl. Mater. Interfaces* **2014**, *6*, 12153.

[9] Y.-K. Hsu, Y.-C. Chen, Y.-G. Lin, *ACS Appl. Mater. Interfaces* **2015**, *7*, 14157.

[10] Q. Liu, F. Cao, F. Wu, W. Tian, L. Li, *RSC Adv.* **2015**, *5*, 79440.

[11] C. Li, X. Zhu, H. Zhang, Z. Zhu, B. Liu, C. Cheng, *Adv. Mater. Interfaces* **2015**, *2*, 1500428.

[12] H. Ishihara, G. K. Kannarpady, K. R. Khedir, J. Woo, S. Trigwell, A. S. Biris, *Phys. Chem. Chem. Phys.* **2011**, *13*, 19553.

[13] M. Chakraborty, D. Roy, A. Biswas, R. Thangavel, G. Udayabhanu, *RSC Adv.* **2016**, *6*, 75063.

[14] C. Chen, H. Bai, Z. Da, M. Li, X. Yan, J. Jiang, W. Fan, W. Shi, *Funct. Mater. Lett.* **2015**, *08*, 1550058.

[15] D. K. Bora, A. Braun, *RSC Adv.* **2014**, *4*, 23562.

[16] M. Shao, F. Ning, M. Wei, D. G. Evans, X. Duan, *Adv. Funct. Mater.* **2014**, *24*, 580.

[17] Y. Li, X. Zhang, S. Jiang, H. Dai, X. Sun, Y. Li, *Sol. Energy Mater. Sol. Cells* **2015**, *132*, 40.

[18] C. Zhang, W. Fan, H. Bai, X. Yu, C. Chen, R. Zhang, W. Shi, *ChemElectroChem* **2014**, *1*, 2089.

[19] S. Hilaire, M. J. Suess, N. Kranzlin, K. Bienkowski, R. Solarska, J. Augustynski, M. Niederberger, *J. Mater. Chem. A* **2014**, *2*, 20530.

[20] A. Wolcott, W. A. Smith, T. R. Kuykendall, Y. Zhao, J. Z. Zhang, *Adv. Funct. Mater.* **2009**, *19*, 1849.

[21] C.-H. Hsu, D.-H. Chen, *Int. J. Hydrogen Energy* **2011**, *36*, 15538.

[22] S. Palmas, P. A. Castresana, L. Mais, A. Vacca, M. Mascia, P. C. Ricci, *RSC Adv.* **2016**, *6*, 101671.

[23] K. Sivula, F. Le Formal, M. Grätzel, *ChemSusChem* **2011**, *4*, 432.

[24] D. Barreca, G. Carraro, A. Gasparotto, C. Maccato, M. E. A. Warwick, K. Kaunisto, C. Sada, S. Turner, Y. Gönüllü, T.-P. Ruoko, L. Borgese, E. Bontempi, G. Van Tendeloo, H. Lemmetyinen, S. Mathur, *Adv. Mater. Interfaces* **2015**, *2*, 1500313.

[25] A. Sheikh, A. Yengantiwar, M. Deo, S. Kelkar, S. Ogale, *Small* **2013**, *9*, 2091.

[26] Y. Guo, Y. Fu, Y. Liu, S. Shen, *RSC Adv.* **2014**, *4*, 36967.

[27] Y. Liu, H. He, J. Li, W. Li, Y. Yang, Y. Li, Q. Chen, *RSC Adv.* **2015**, *5*, 46928.

[28] R. Solarska, K. Bieńkowski, A. Królikowska, M. Dolata, J. Augustyński, *Funct. Mater. Lett.* **2014**, *07*, 1440006.

[29] R. Solarska, R. Jurczakowski, J. Augustynski, *Nanoscale* **2012**, *4*, 1553.

[30] T. Zhu, M. N. Chong, E. S. Chan, *ChemSusChem* **2014**, *7*, 2974.

[31] Y. Mao, Y. Cheng, J. Wang, H. Yang, M. Li, J. Chen, M. Chao, Y. Tong, E. Liang, *New J. Chem.* **2016**, *40*, 107.

[32] Y. Qiu, K. Yan, H. Deng, S. Yang, *Nano Lett.* **2012**, *12*, 407.

[33] R. Lv, T. Wang, F. Su, P. Zhang, C. Li, J. Gong, *Nano Energy* **2014**, *7*, 143.

[34] N. Chouhan, C. L. Yeh, S. F. Hu, J. H. Huang, C. W. Tsai, R. S. Liu, W. S. Chang, K. H. Chen, *J. Electrochem. Soc.* **2010**, *157*, B1430.

[35] Y. Liu, L. Sun, J. Wu, T. Fang, R. Cai, A. Wei, *Mater. Sci. Eng., B* **2015**, *194*, 9.

[36] S.-M. Lam, J.-C. Sin, A. Z. Abdullah, A. R. Mohamed, *Ceram. Int.* **2013**, *39*, 2343.

[37] J. Xie, Z. Zhou, Y. Lian, Y. Hao, X. Liu, M. Li, Y. Wei, *Ceram. Int.* **2014**, *40*, 12519.

[38] F. Zheng, H. Lu, M. Guo, M. Zhang, Q. Zhen, *J. Mater. Chem. C* **2015**, *3*, 7612.

[39] M. Wang, C. Chen, H. Qin, L. Zhang, Y. Fang, J. Liu, L. Meng, *Adv. Mater. Interfaces* **2015**, *2*, 1500163.

[40] L. Cai, F. Ren, M. Wang, G. Cai, Y. Chen, Y. Liu, S. Shen, L. Guo, *Int. J. Hydrogen Energy* **2015**, *40*, 1394.

[41] M. Wang, F. Ren, J. Zhou, G. Cai, L. Cai, Y. Hu, D. Wang, Y. Liu, L. Guo, S. Shen, *Sci. Rep.* **2015**, *5*, 12925.

[42] L. Yan, W. Zhao, Z. Liu, *Dalton Trans.* **2016**, *45*, 11346.

[43] C. K. Chen, Y.-P. Shen, H. M. Chen, C.-J. Chen, T.-S. Chan, J.-F. Lee, R.-S. Liu, *Eur. J. Inorg. Chem.* **2014**, *2014*, 773.

[44] S.-M. Lam, J.-C. Sin, A. Z. Abdullah, A. R. Mohamed, *Sep. Purif. Technol.* **2014**, *132*, 378.

[45] H. Kim, M. Seol, J. Lee, K. Yong, *J. Phys. Chem. C* **2011**, *115*, 25429.

[46] D. Li, H. Haneda, N. Ohashi, S. Hishita, Y. Yoshikawa, *Catal. Today* **2004**, *93–95*, 895.

[47] G. Carraro, C. Maccato, A. Gasparotto, K. Kaunisto, C. Sada, D. Barreca, *Plasma Processes Polym.* **2016**, *13*, 191.

[48] C. Jiang, S. J. A. Moniz, M. Khraisheh, J. Tang, *Chem. Eur. J.* **2014**, *20*, 12954.

[49] S. Sakthivel, S. U. Geissen, D. W. Bahnemann, V. Murugesan, A. Vogelpohl, *J. Photochem. Photobiol., A* **2002**, *148*, 283.

[50] K. Karthick, K. Vijayalakshmi, *J. Mater. Sci. - Mater. Electron.* **2015**, *26*, 7255.

[51] A. J. T. Naik, I. P. Parkin, R. Binions, *IEEE Sens. J.* **2014**, *14*, 3137.

[52] S. Park, T. Hong, J. Jung, C. Lee, *Curr. Appl Phys.* **2014**, *14*, 1171.

[53] D. Barreca, G. Carraro, A. Gasparotto, C. Maccato, C. Sada, E. Bontempi, M. Brisotto, O. Pliekhova, U. L. Štangar, *Environ. Sci. Pollut. Res.* **2016**, *23*, 20350.

[54] D. Barreca, G. Carraro, A. Gasparotto, C. Maccato, M. E. A. Warwick, E. Toniato, V. Gombac, C. Sada, S. Turner, G. Van Tendeloo, P. Fornasiero, *Adv. Mater. Interfaces* **2016**, *3*, 1600348.

[55] G. Carraro, C. Maccato, A. Gasparotto, M. E. A. Warwick, C. Sada, S. Turner, A. Bazzo, T. Andreu, O. Pliekhova, D. Korte, U. Lavrenčič Štangar, G. Van Tendeloo, J. R. Morante, D. Barreca, *Sol. Energy Mater. Sol. Cells* **2017**, *159*, 456.

[56] G. Carraro, A. Gasparotto, C. Maccato, E. Bontempi, F. Bilo, D. Peeters, C. Sada, D. Barreca, *CrystEngComm* **2014**, *16*, 8710.

[57] PDF card No. 36-1451.

[58] D. Barreca, A. P. Ferrucci, A. Gasparotto, C. Maccato, C. Maragno, E. Tondello, *Chem. Vap. Deposition* **2007**, *13*, 618.

[59] D. Bekermann, A. Ludwig, T. Toader, C. Maccato, D. Barreca, A. Gasparotto, C. Bock, A. D. Wieck, U. Kunze, E. Tondello, R. A. Fischer, A. Devi, *Chem. Vap. Deposition* **2011**, *17*, 155.

[60] D. Briggs, M. P. Seah, *Practical surface analysis: Auger and X-ray photoelectron spectroscopy*, John Wiley & Sons: New York, 2nd ed., 1990.

[61] J. F. Moulder, W. F. Stickle, P. E. Sobol, K. D. Bomben, *Handbook of X-ray photoelectron spectroscopy*, Perkin Elmer Corporation, Eden Prairie, MN, USA, 1992.

[62] PDF card No. 39-1346.

[63] Y. Wang, L. Cai, Y. Li, Y. Tang, C. Xie, *Physica E* **2010**, *43*, 503.

[64] A. R. Phani, M. Passacantando, L. Lozzi, S. Santucci, *J. Mater. Sci.* **2000**, *35*, 4879.

[65] K.-S. Ahn, S. Shet, T. Deutsch, C.-S. Jiang, Y. Yan, M. Al-Jassim, J. Turner, *J. Power Sources* **2008**, *176*, 387.

[66] D. Barreca, G. Carraro, A. Gasparotto, C. Maccato, C. Sada, A. P. Singh, S. Mathur, A. Mettenbörger, E. Bontempi, L. E. Depero, *Int. J. Hydrogen Energy* **2013**, *38*, 14189.

[67] P. Schlossmacher, D. O. Klenov, B. Freitag, H. S. von Harrach, *Micros. Today* **2010**, *18*, 14.

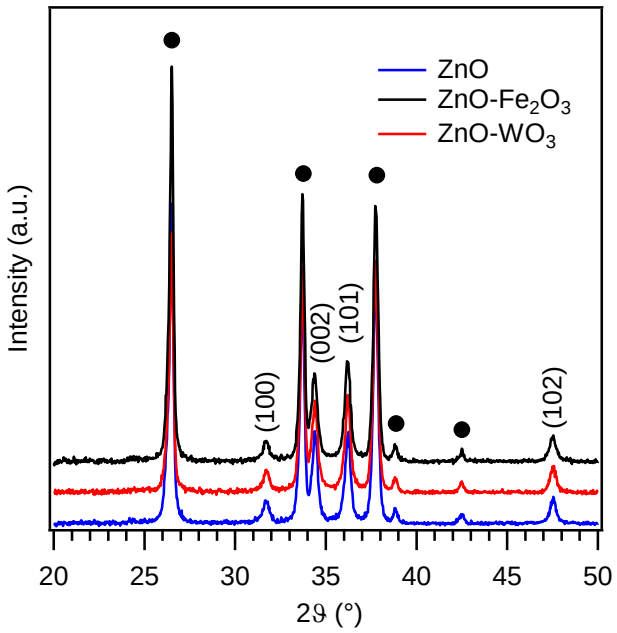

Figure 1. GIXRD patterns of ZnO, ZnO-Fe_2O_3 and ZnO-WO_3 deposits. For sake of clarity, patterns have been vertically shifted and peaks pertaining to the FTO-coated glass substrate marked by black circles. Indexed peaks correspond to *wurtzite* ZnO reflections.

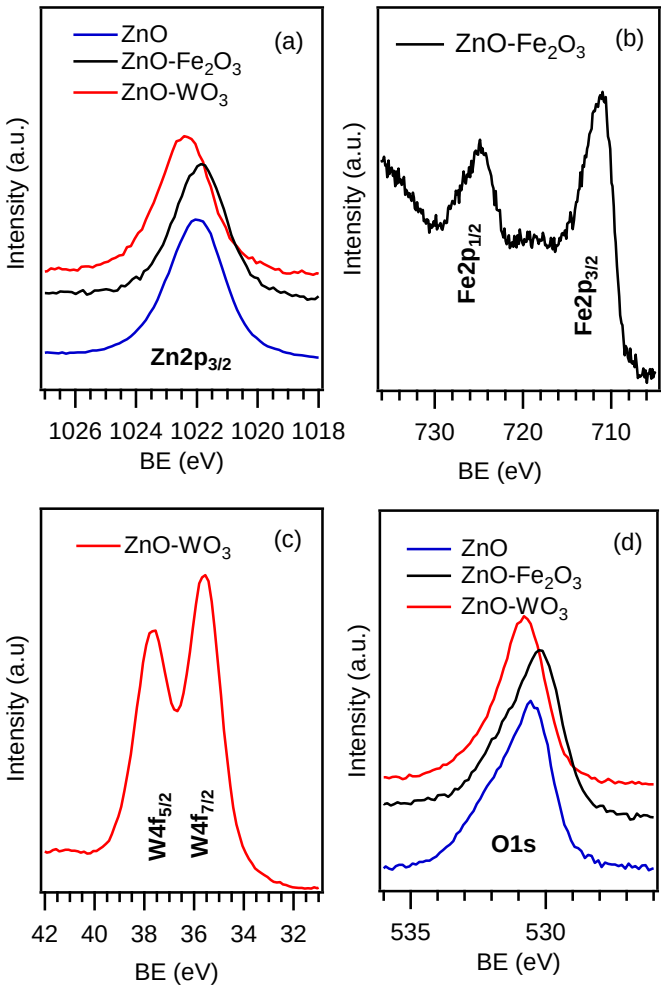

Figure 2. Surface $Zn2p_{3/2}$ (a), Fe2p (b), W4f (c), and O1s (d) photoelectron peaks for the fabricated specimens.

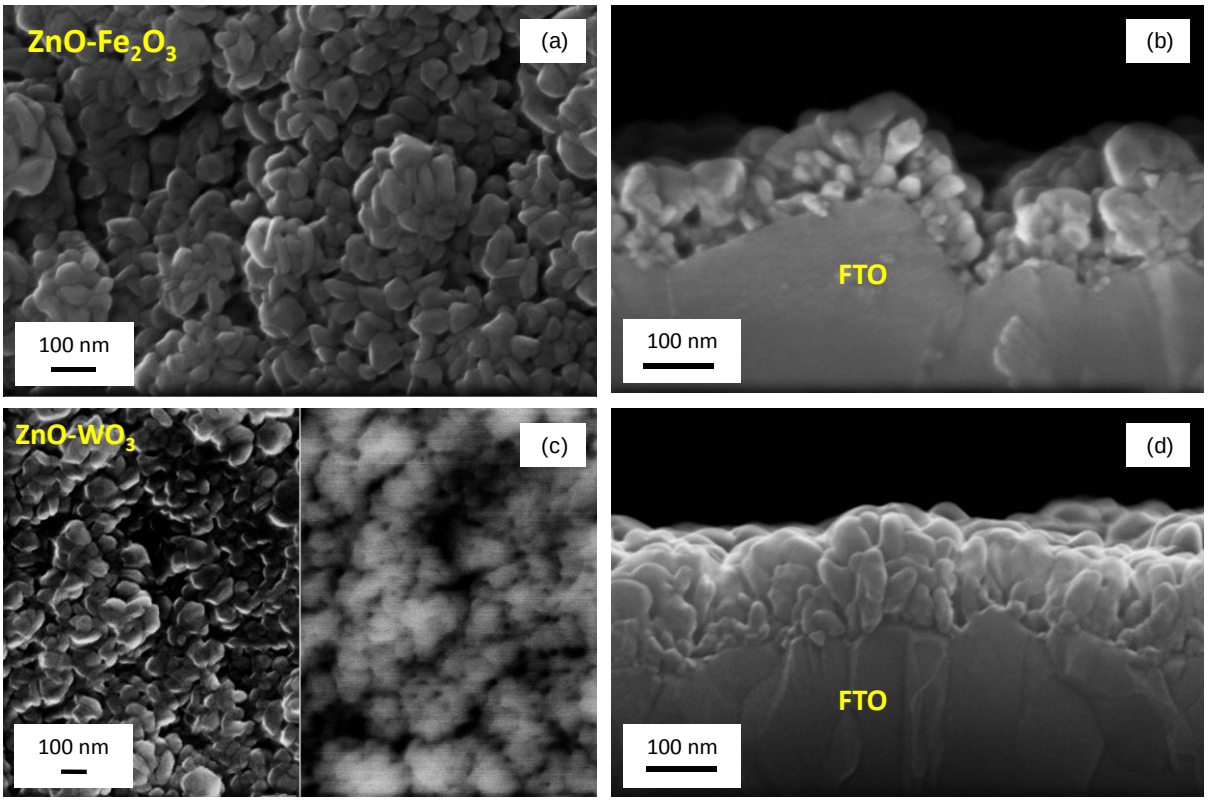

Figure 3. Plane-view (a,c) and cross-sectional (b,d) FE-SEM images for the fabricated composite specimens. For the ZnO-WO_3 sample the left and right plane-view micrographs were recorded using in-lens and back-scattered electrons, respectively.

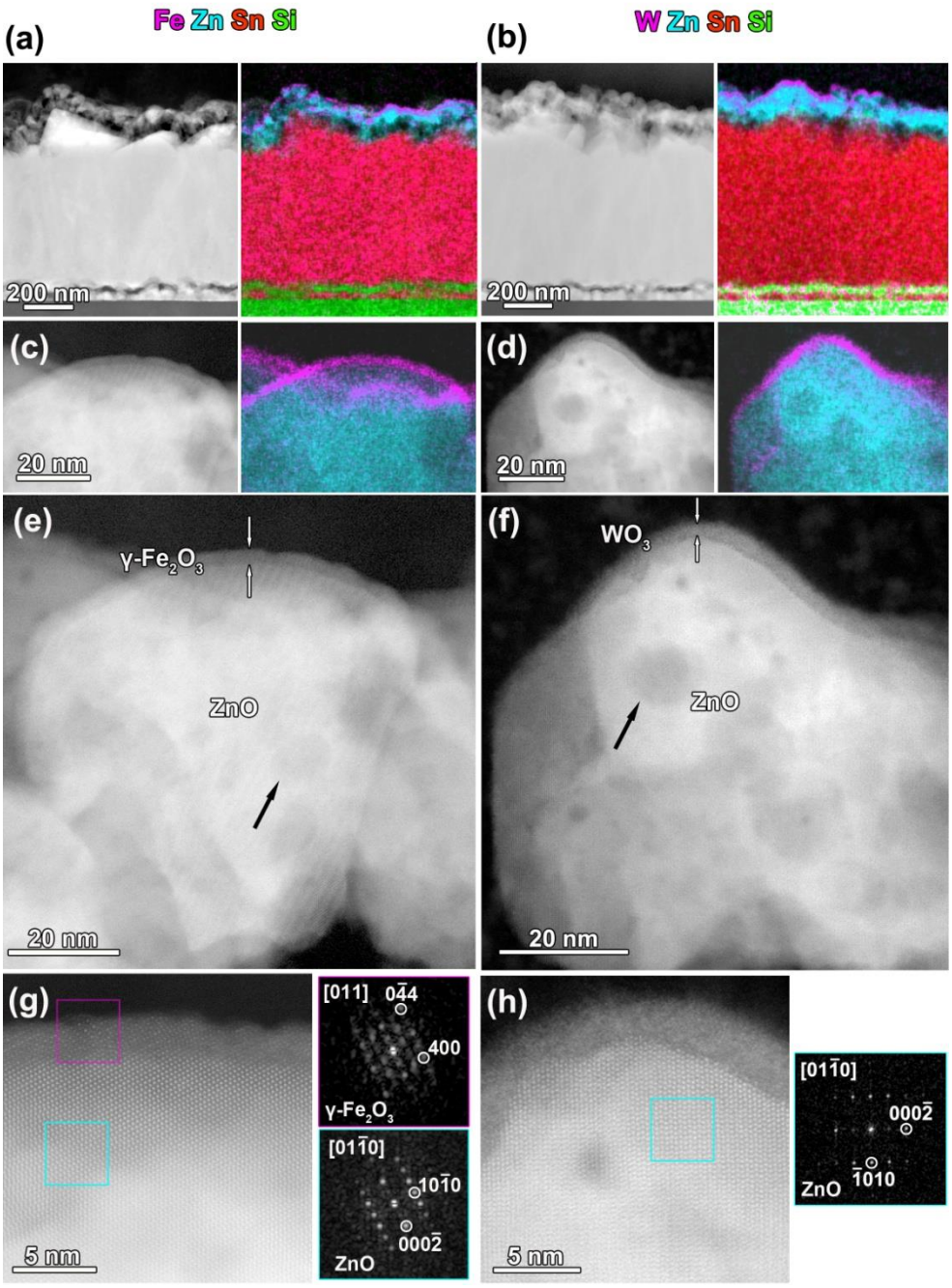

Figure 4. Cross sectional HAADF-STEM images and corresponding EDXS elemental maps for ZnO-Fe_2O_3 (a) and ZnO-WO_3 (b) nanodeposits. (c-f) High magnification images of ZnO-Fe_2O_3 and ZnO-WO_3 interface, together with EDXS elemental maps. Black arrows indicate the positions of dark-contrast voids in the ZnO crystals, whereas surface Fe_2O_3 and WO_3 layers are indicated by white arrows. (g-h) High resolution STEM images of the interface between ZnO-Fe_2O_3 and ZnO-WO_3 and corresponding FFT patterns. ZnO crystals are oriented along the [01 $\bar{1}$ 0] zone axis.

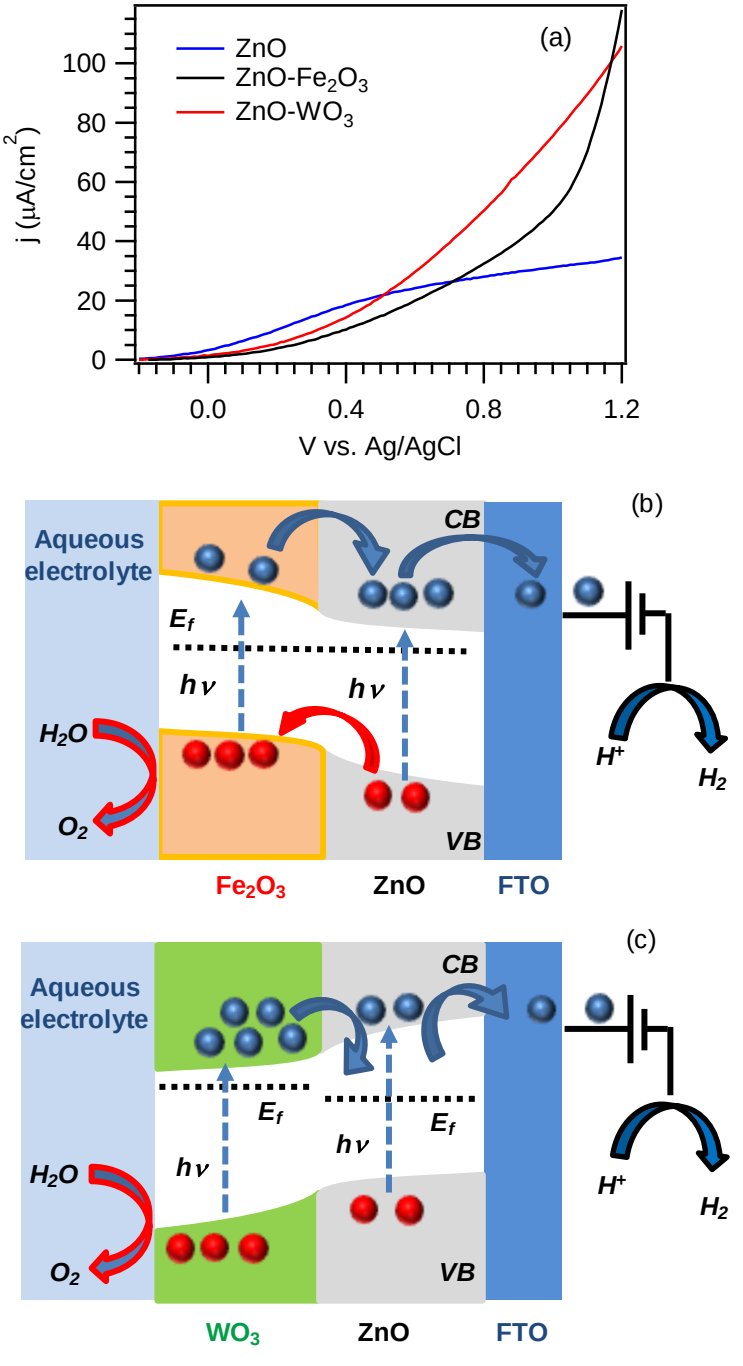

Figure 5. (a) Photocurrent density *vs.* applied potential curves for the target systems, recorded in 0.5 M Na_2SO_4 under simulated solar illumination. Schematic energy level diagrams for: (b) ZnO-Fe_2O_3, and (c) ZnO-WO_3 systems, showing the photoactivated charge transfer processes occurring upon operation.

Table of contents entry

Keywords: ZnO; Fe_2O_3; WO_3; nanoheterostructures; water splitting; photoelectrochemistry.

Vapor phase fabrication of nanoheterostructures based on ZnO for photoelectrochemical water splitting

Davide Barreca, Giorgio Carraro, Alberto Gasparotto, Chiara Maccato, Thomas Altantzis, Cinzia Sada, Kimmo Kaunisto, Tero-Petri Ruoko, and Sara Bals

ZnO-Fe_2O_3 and ZnO-WO_3 nanoheterostructures, consisting of Zn(II) oxide porous deposits conformally covered by iron or tungsten oxide overlayers, are developed by a hybrid synthetic strategy combining chemical vapour deposition and sputtering processes. The target systems are characterized in detail and investigated as anodes for photoelectrochemical water splitting, a critical research area promising the efficient conversion of solar energy into chemical fuels.